Three-dimensional tracking of single mRNA particles in *Saccharomyces cerevisiae* using a double-helix point spread function

Michael A. Thompson[a], Jason M. Casolari[b,c], Majid Badieirostami[a], Patrick O. Brown[b,c], and W. E. Moerner[a,1]

[a]Department of Chemistry, Stanford University, Stanford, CA 94305-5080; [b]Howard Hughes Medical Institute; and [c]Department of Biochemistry, Stanford University, Stanford, CA 94305-5080

This contribution is part of the special series of Inaugural Articles by members of the National Academy of Sciences elected in 2007.

Contributed by W. E. Moerner, August 30, 2010 (sent for review August 1, 2010)

Optical imaging of single biomolecules and complexes in living cells provides a useful window into cellular processes. However, the three-dimensional dynamics of most important biomolecules in living cells remains essentially uncharacterized. The precise subcellular localization of mRNA-protein complexes plays a critical role in the spatial and temporal control of gene expression, and a full understanding of the control of gene expression requires precise characterization of mRNA transport dynamics beyond the optical diffraction limit. In this paper, we describe three-dimensional tracking of single mRNA particles with 25-nm precision in the *x* and *y* dimensions and 50-nm precision in the *z* dimension in live budding yeast cells using a microscope with a double-helix point spread function. Two statistical methods to detect intermittently confined and directed transport were used to quantify the three-dimensional trajectories of mRNA for the first time, using *ARG3* mRNA as a model. Measurements and analysis show that the dynamics of *ARG3* mRNA molecules are mostly diffusive, although periods of non-Brownian confinement and directed transport are observed. The quantitative methods detailed in this paper can be broadly applied to the study of mRNA localization and the dynamics of diverse other biomolecules in a wide variety of cell types.

3D microscopy | single molecule | superresolution | single particle tracking

Since the first optical detection and spectroscopy of single molecules in condensed phases in 1989 (1), optical imaging of single biomolecules and complexes in living cells has become widespread and continues to provide a useful window into a variety of cellular processes (2–5). Among the various methods of extracting information from single-molecule measurements such as FRET, fluctuations, polarization, and so on, single-particle tracking (SPT) is relatively straightforward to implement with two-dimensional wide-field imaging and simply involves optical measurement of the (x,y) position of the single object as a function of time as a probe of diffusion or transport. Two-dimensional SPT was applied to multiply labeled fluorescent LDL particles (6) and to kinesin-driven beads (7) in the 1980s. The technique entered the single-fluorophore regime in measurements of the mobility of lipid probes in a supported lipid bilayer (8). Two-dimensional SPT has seen application in a variety of studies of transmembrane proteins and other membrane structures in cells (9–19), and much theoretical effort has been directed toward the analysis of 2D diffusion in biological environments of varying complexity (20–24). However, within a cell, two-dimensional tracking studies will always lack information because of the inherently three-dimensional nature of the motion; therefore, a method to track particles in three dimensions is needed. Recently, the double-helix point spread function (DH-PSF) microscope has been shown to provide 3D position information beyond the optical diffraction limit from standard wide-field microscopy of single molecules and point emitters (25–27). By use of image processing with a spatial light modulator (SLM), the DH-PSF converts the normal single fluorescence spot from a single emitter into two spots. Different z positions are then sensed by the DH-PSF imaging system as different angles between the two spots. The two spots spin about one another for single emitters at different axial positions over a 2-μm range, effectively carving out a double helix along the z axis.

The localization of mRNA-protein (mRNP) complexes to specific subcellular compartments allows for greater spatial and temporal control of gene expression (28). Indeed specific subcellular localization may be a genetically encoded feature of the expression program of most, and perhaps all, mRNAs in complex organisms (29, 30). Central to the understanding of the mechanisms of mRNA localization is the study of the dynamics of the transport. Many different modes of transport have been reported, including directed motion (31), diffusion (32), and trapping. In this study, we examine mRNA localization in *Saccharomyces cerevisiae*, a model eukaryotic organism amenable to optical imaging and with exceptionally well-developed tools for genetic manipulation. Using a DH-PSF microscope, we track the dynamics of mRNPs at high spatial and temporal resolution in three dimensions in living yeast cells. We describe two quantitative, unbiased techniques to detect and measure nonrandom confinement and directed motion, which we used to study the motion of a nonlocalized mRNP.

The dynamics of only one mRNA in yeast, *ASH1*, have been studied extensively. Using MS2-GFP tagging of a chimeric mRNA comprising a reporter gene and the *ASH1* 3′-UTR, Bertrand et al. (33) observed random movement of the *ASH1* chimeric transcript with a bias toward movement to the bud. Time-lapse movies of its motion allowed for an estimate of *ASH1* velocity, presumably reflecting the stepping rate of the actomyosin protein, Myo4, that was found to be necessary for appropriate *ASH1* localization. Indeed, deletion of *MYO4* caused the *ASH1* chimera to become immobile or to demonstrate short movements lacking persistence (33). Although studies of factors that affect *ASH1* localization and translation have continued (34, 35), little is known about the dynamic behavior of other mRNAs or mRNPs. In the past decade, advances in single-molecule imaging as well as the efficient tagging of endogenous mRNAs now provide a unique opportunity to study the dynamic behavior of mRNPs in living cells with extraordinarily high spatial and temporal resolution.

Author contributions: M.A.T., J.M.C., P.O.B., and W.E.M. designed research; M.A.T. and J.M.C. performed research; M.A.T. and M.B. contributed new reagents/analytic tools; M.A.T. analyzed data; and M.A.T., J.M.C., P.O.B., and W.E.M. wrote the paper.

The authors declare no conflict of interest.

Freely available online through the PNAS open access option.

[1]To whom correspondence may be addressed at: Department of Chemistry Mail Code 5080, Stanford, CA 94305-5080. E-mail: wmoerner@stanford.edu.

This article contains supporting information online at www.pnas.org/lookup/suppl/doi:10.1073/pnas.1012868107/-/DCSupplemental.

This work is focused on the dynamics of the *ARG3* mRNA, which encodes ornithine carbamoyltransferase, an enzyme that catalyzes the sixth step in the biosynthesis of the arginine precursor ornithine. *ARG3* was chosen because it encodes a housekeeping enzyme that is not known to exhibit asymmetric localization in the cytoplasm, providing a benchmark and point of reference for future studies of localized mRNPs. Furthermore, *ARG3* is expressed at just 1–2 copies per cell (36, 37), thus reducing the potential obfuscation of high-confidence single trajectories by the interference of overlapping signals from distinct particles. To visualize the mRNPs, we used a labeling scheme based upon that of Haim et al. (38) The *ARG3* mRNA was engineered with 12 bacteriophage MS2 hairpin loops, which provide high-affinity binding sites for the MS2 coat protein, incorporated between the coding sequence and the 3′ UTR. Integration of the MS2 coat-protein binding elements into the native *ARG3* locus allows for expression of the mRNA of interest from its own promoter and thus at native levels. Additionally, retention of the native 3′ UTR sequence, which in many genes encodes mRNA localization information, minimizes the risk that the MS2 hairpins might alter the wild-type dynamics of the mRNA. The strain containing this tagged *ARG3* gene also carries a methionine-inducible gene encoding the MS2 coat protein fused to three tandem copies of the EGFP coding sequence. Each *ARG3* mRNA can bind up to 12 MS2 proteins, recruiting up to 36 EGFPs, enabling it to be visualized as a bright spot over the background fluorescence of unbound cytoplasmic MS2-3xEGFP. The MS2 coat protein we used in this study lacks the nuclear localization sequence to avoid any confounding effects of the nuclear import machinery on the observed dynamics (33, 39).

There are many considerations in selecting a method for 3D particle tracking. In one approach, the microscope is locked to the particle position and the sample stage moves to follow the motion of the particle (40–42); these methods have the advantage of large axial range but can track only one object at a time. In cellular transport studies, it is often useful to study the cotransport of other structures in the cell that are related to the transport of mRNPs as well as different mRNPs at the same time, so a method with the capability of multiobject imaging would be important. Wide-field techniques for 3D SPT that do not require stage motion have also been described, including multiplane tracking (43), astigmatism (44), and parallax (45). The wide-field DH-PSF imaging method was chosen for this study for two main reasons. The first is the high localization precision available given a low photon budget (27). Tracking with 25-nm precision in the x and y dimensions and 50 nm in the z dimension is possible despite the inherently low signal-to-background imaging conditions associated with the MS2 labeling scheme (33). The second and perhaps more important reason is that the DH-PSF is superior to the other wide-field techniques because of the large 2-μm depth of field, which translates to a constant localization precision over a 2-μm z range. This corresponds to being able to follow dynamics throughout approximately one-half of the size of a typical haploid yeast cell. Three-dimensional mRNP tracking has been demonstrated previously (39), although the focus of that work was on the cotransport of two localized mRNAs, and only one three-dimensional trajectory was presented.

Particle tracking studies yield position information as a function of time, and reliable conclusions from these data depend on statistical analysis. We developed two methods to quantitatively detect both confined and directed motion in 3D, extending mathematical approaches used in previous 2D membrane studies. The first, called the speed correlation index (SCI), first developed by Bouzigues and Dahan (24), provides a measure of the "directedness" of a portion of a single-particle trajectory by comparing the velocity correlations in the observed data to those of a Brownian particle. By using a three-dimensional SCI, we can extract velocities from directed portions of trajectories as well as the amount of time that each particle spends in a directed state. In this study, we evaluated the dependence of the putative directed motion on the actin cytoskeleton by examining the effect of disrupting actin filaments by addition of latrunculin B (46, 47).

To study the dynamic confinement of the mRNPs, we devised a 3D confinement index based on a two-dimensional criterion developed by Saxton, and Jacobsen and coworkers (21, 48). This confinement index was then used to measure the decidedly nonrandom confinement dynamics of *ARG3* mRNPs, allowing us to estimate the size of the confinement region as well as the time that the mRNP spends in each confining region. These tests, combined with DH-PSF imaging, provide a powerful method to understand mRNP dynamics that should be adaptable to many different mRNP labeling schemes and diverse organisms.

Results and Discussion

The utility of the DH-PSF imaging system in measuring the three-dimensional trajectories of mRNPs is illustrated in Fig. 1. Because yeast cells are round, three-dimensional measurements are essential to extract full information about the dynamics of the system. In the trajectory displayed in Fig. 1*B*, the two-dimensional projection fails to reveal the directed motion in z occurring approximately from 5 to 7 s. In fact, because of the much smaller magnitude of lateral motion during this time, the two-dimensional trajectory might erroneously be described as being confined or corralled. Central to this study is our effort to accurately categorize the dynamics and, more importantly, the switching between different modes of motion, which would be impossible in a two-dimensional representation as shown by the difference between Fig. 1*B* and Fig. 1*C*. In the raw fluorescence images in Fig. 1*D*, the mRNP appears as two bright dots above a diffuse green background as expected from the DH-PSF. The different images are of different time points and thus different z positions in the trajectory in Fig. 1*C*.

Even though the motion of a single mRNP in a cell can be quite complicated, it is useful to start with a simple Brownian model to initially characterize the dynamics of the mRNPs. Because the mRNPs are imaged on top of a bright background of diffusing MS2-3xEGFP, the signal to background in these experiments is quite low. Therefore, one must take into account both static errors (localization precision arising mainly from the limited number of detected photons) and dynamic errors (arising from motion during the acquisition time) in the localization of the particles. For a particle undergoing Brownian motion being tracked by an imaging system with exposure time, Δt, and localization precision, σ, the three-dimensional mean-squared displacement (MSD) as a function of time lag, τ, can be written as

$$\langle \Delta r^2 \rangle = 6D(\tau - \Delta t/3) + 2\sum_{i=1}^{3} \sigma_i^2, \qquad [1]$$

where D is the diffusion coefficient, and σ_i is the localization precision in the ith dimension (23). Even though the mRNPs studied in this paper show a wide variety of diffusive, confined, and directed motions, at short-time lags (<0.1 s), the dynamics appear diffusive and the corresponding MSD curve is linear with a y intercept given by Eq. **1** (see *SI Text* for an example). Using Eq. **1**, it is possible to also derive the localization precision σ_i for each trajectory. The mean values of the localization precisions in x, y, and z extracted from 267 trajectories are 24.7, 27.9, and 49.5 nm, respectively. More details about the localization precision, numbers of detected photons, and signal to background of these measurements can be found in *SI Text*.

Thirty-six of the 267 *ARG3* mRNP particle trajectories we analyzed, or 13%, exhibited no measurable movement above the detection limit. Particles with MSD values at the eighth time lag point no greater than the average squared 3D localization precision $\bar{\sigma}_{3D}{}^2 = \bar{\sigma}_x^2 + \bar{\sigma}_y^2 + \bar{\sigma}_z^2$ in these experiments (0.0038 μm^2)

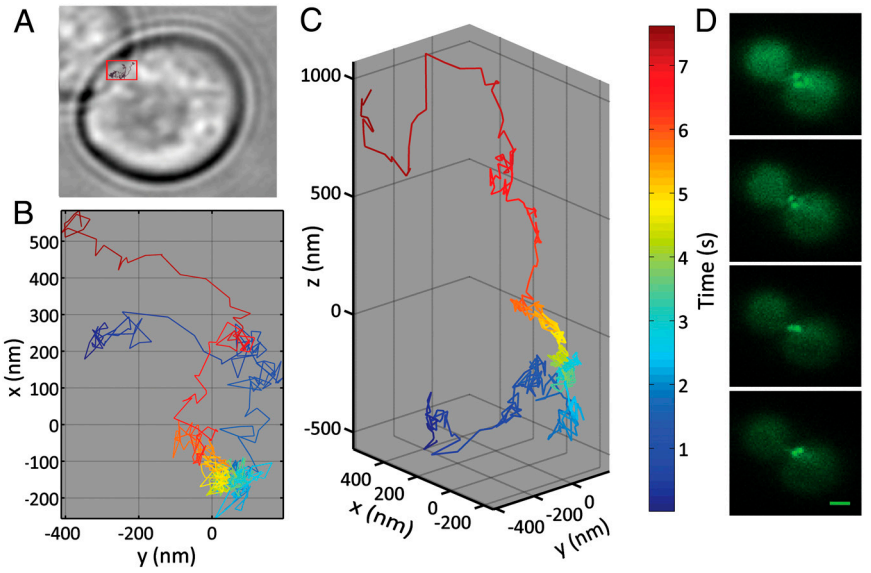

Fig. 1. Single mRNPs can be tracked in three dimensions by using a microscope that exhibits a DH-PSF. (*A*) White light transmission image of a yeast cell with a second cell to the upper left. The trajectory in *B* is superposed on the image in the top left of the cell (outlined in red). (*B*) Two-dimensional projection of the trajectory in *A*. Time is encoded as color (see color bar to the right of *C*), with 15-ms integration time for each point. (*C*) Actual three-dimensional motion for the trajectory shown in *B*. Note the apparent directed motion in *z* that is not apparent in *B*. (*D*) Raw data from the DH-PSF microscope showing the mRNA as two bright dots on top of a diffuse background arising from MS2-EGFP being expressed in the cytoplasm. (*Top* to *Bottom*) Time when each image was taken was 0, 0.233, 5.78, and 6.99 s. Scale bar is 2 μm.

were classified as stationary and were excluded from both the diffusion analysis and the analysis of directed motion and confinement presented below. We never observed particles going from completely stationary to diffusive movement. We analyzed the cellular locations of the stationary particles by aligning the fluorescence images with white light images; 24 (67%) were localized to the cortex and 12 (33%) were found in the interior of the cell. This asymmetric distribution suggests that movement of these mRNPs may be restricted by interactions with a structure at the cell cortex.

Characterizing Diffusion

Single mRNA particles may show complex trajectories with varying modes of movement that cannot be fit to simple models. Nevertheless, it is useful to contrast their movements to Brownian motion. The short-time mean diffusion coefficient for a single trajectory can be measured by extracting the local slope of the linear fit of the MSD to Eq. **1**. The choice of how many time points to include in the calculation can affect the results and should be considered carefully (49, 50). In this study, the first 8 time-lag points in the MSD were used to calculate the diffusion coefficient. Using the first 4 time lags to extract the diffusion coefficient gave similar results to choosing 8 time-lag points. Choosing 16 time lags greatly increased the number of low diffusion coefficients because the effects of confinement become apparent at longer lag times. Diffusion coefficients were calculated based on the entire trajectory of each particle (hundreds of time points in length, vide infra), for 231 *ARG3* mRNP particles (Fig. 2*A*); the diffusion coefficients can therefore be understood as the mean values for the entire observed trajectory of each particle. A trajectory had to be at least 50 time points in length to calculate a value for *D*. As discussed below, these particles displayed a variety of movement behaviors during the periods of observation. Regardless, the distribution of mean diffusion coefficients conveys useful information about the heterogeneity observed from particle to particle.

The mean ensemble diffusion coefficient from this analysis was 0.039 $\mu m^2/s$, which is consistent with previous measurements in other organisms (32, 33, 51). The peak of the distribution, which is more representative of the majority of behaviors, was 0.018 $\mu m^2/s$. The highest diffusion coefficient observed was 0.40 $\mu m^2/s$. For a homogenous population of Brownian particles with diffusion coefficients measured by finding the slope of the MSD, a characteristic distribution of experimentally observed diffusion coefficients is expected due to limited numbers of position measurements (20, 22, 49). The observed distribution of *D* values shown in Fig. 2 is far broader than a simulated Brownian distribution with excess density at larger values of *D* (see *SI Text*). Although a distribution of diffusion coefficients for mRNPs in yeast has not, to our knowledge, been previously reported, there are two well-established reasons to expect a broad distribution of diffusion coefficients: first, the heterogeneity of the mRNPs themselves, and second, the heterogeneity of the cellular environment. Because the *ARG3* mRNPs we studied most likely comprise not single mRNAs, but a conglomeration of one or more mRNA molecules, ribosomes, RNA-binding proteins, and other mRNP associated entities (52), it is reasonable to expect a wide variety of particle sizes, and thus, a variety of diffusion coefficients.

Variation in the apparent brightness of the particles, which is roughly proportional to the number of EGFP units bound, provides evidence for particle heterogeneity; precise counting of the number of EGFPs is not the goal here (53). To carefully measure the photon emission rate of the particles, the phase modulation of the spatial light modulator was turned off and the mRNPs were imaged in standard 2D wide-field epifluorescence mode. In a histogram of particle brightness measured in absolute numbers of photons detected above background per 15-ms image (Fig. 2*B*), a peak at around 2,500 photons/15 ms is likely to represent single *ARG3* mRNA molecules with ~36 bound EGFPs. (For more details on the photon counting in Fig. 2*B*, see *SI Text*.) Particles

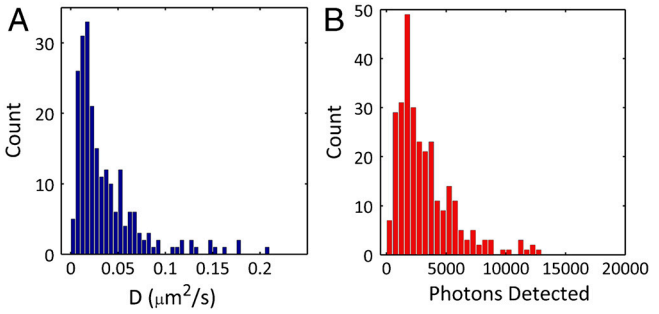

Fig. 2. Heterogeneous distribution of diffusive behaviors and brightness of *ARG3* mRNP particles. (*A*) Distribution of diffusion coefficients for 231 mRNA trajectories. The average trajectory length used to calculate *D* was 673 time steps. The mean diffusion coefficient was 0.040 $\mu m^2/s$; the peak of the distribution is 0.018 $\mu m^2/s$. This distribution is much broader than that of a homogenously diffusing particle (see text, *SI Text*). (*B*) Particle brightness distribution for each 15-ms imaging frame with the SLM off ; the large peak at 2,500 photons likely represents particles with ~36 EGFPs. Note that many particles have much higher photon counts; they presumably represent mRNPs containing more than one *ARG3* mRNA.

with higher photon counts therefore suggest mRNPs containing more than one labeled *ARG3* mRNA molecule (39). This wide distribution of particle brightness and the heterogeneity in apparent diffusion coefficient (Fig. 2*A*) may both be due in part to heterogeneous mRNP composition and stoichiometry.

Classifying Changes in mRNP Motion

In the above discussion the average values of parameters such as the diffusion coefficient and localization precision were measured from entire trajectories, where each trajectory gives one diffusion coefficient and one localization precision. Although time-average quantities from each trajectory can be used to assess global heterogeneity, we seek a deeper picture of the mRNP dynamics. The trajectories lasted on average for 673 time steps or 10.1 s, which was long enough to observe switching between different modes of transport. By analyzing the behavior of each individual trajectory we were able to objectively classify intervals of dynamic behavior of each particle into one of three main modes, (*i*) confined (or stationary), (*ii*) directed, or (*iii*) diffusive. The two tests we used to define periods of confinement and directed transport, respectively, were each based on cutting a long trajectory into much shorter subtrajectories that were then subjected to a statistical test comparing the observed behavior to a null hypothesis. For both cases, the null hypothesis was a simulated three-dimensional unobstructed Brownian random walk with an average D and localization precision identical to the measured values for the corresponding experimental trajectory. As a probability threshold for classifying a behavior as deviating from the null model, we required that only 5% of the simulated Brownian trajectories would have been incorrectly characterized as confined or directed, respectively. Clearly, one could apply even more complex statistical analysis to the three-dimensional trajectories obtained using the DH-PSF, especially the apparently diffusive subtrajectories. For example, by using a maximum likelihood estimation scheme rather than fitting the MSD, one can more accurately sense changes in D as a function of time (50). One could also further analyze the periods of anomalous subdiffusive movement (sublinear time-lag dependence of the MSD) to understand the finer details of the cellular environment (54, 55).

The human brain is notoriously effective at identifying patterns; even when looking at completely random Brownian-motion trajectories, an observer will commonly identify areas of apparently "directed" or "confined" motion (22). Regardless of the type of transport, objective classification of behaviors therefore requires tests that do not rely on human discernment. We therefore developed two explicit, objective statistical tests to detect and quantify the switching of a single trajectory between directed and confined modes of motion. A specific example of a trajectory that switches between all three different modes of motion is discussed in *SI Text*).

In total, 2,695 s of mRNP transport were observed. Of those, 163 s (6%) were confined, 410 s (15%) were stationary, 105 s (4%) were directed, and the remaining 2,017 s (75%) were classified by default as consistent with diffusion. The stationary and confined behaviors are not necessarily different, because the particle being denoted stationary means that it did not detectably move during the observation time. The absolute numbers given above, although objective and useful in distinguishing gross differences in behavior (51, 53), are not precisely robust or generalizable because they depend heavily on chosen thresholds and tests. These types of categorizations are nevertheless useful for comparing mRNPs or conditions in the same experiment, using the same set of tests and thresholds.

Directed Motion

Directed motion has been reported in several studies of mRNP dynamics (31, 33, 53). Reliable detection of directed motion is not trivial, because Brownian motion can occasionally give rise to fluctuations that can appear to be directed. Many of the trajectories observed in this study have intervals of apparently directed (asymmetric) movement, with a characteristic quadratic time-lag dependence in the MSD curve (56) (Fig. 3). To objectively and quantitatively identify intervals of directed motion and measure the dynamics of particles moving in and out of directed modes of motion, we developed a modified three-dimensional version of the SCI approach of Bouzigues and Dahan (24). The SCI value is the normalized velocity autocorrelation function at the first time lag calculated over a selected region of the trajectory. The SCI uses the fact that velocity correlations vanish for Brownian motion but have a constant positive value for directed motion. A completely directed trajectory will have an SCI value of 1, whereas a completely random trajectory with a localization precision of 0 will have on average an SCI value of 0. A threshold value of the SCI can be set such that only 5% of Brownian trajectories generated by Monte Carlo simulations with the same short-time diffusion coefficient and localization precision are misclassified as directed (Fig. 3*C*). When an observed SCI exceeds the threshold, that portion of the trajectory is classified

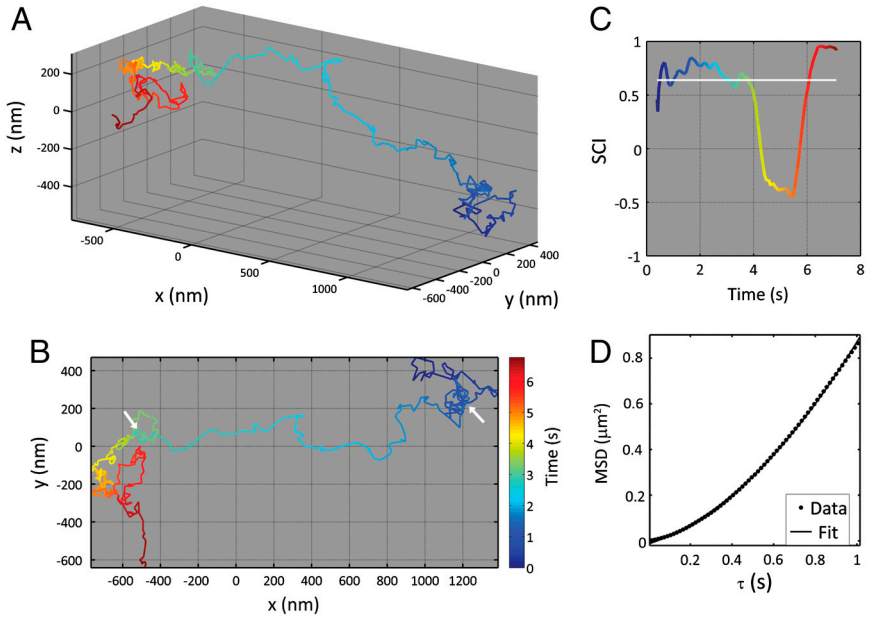

Fig. 3. Detection and quantification of three-dimensional directed motion in an experimental trajectory. (*A*) Three-dimensional trajectory consisting of 500 time points. Time is encoded as the color of the trajectory going from blue to red. (*B*) Two-dimensional projection of the data in *A*. The white arrows denote the start and end of the directed portion of the trajectory. (*C*) Plot of the speed correlation index as a function of time. The white line represents the SCI threshold such that if the observed SCI falls above the threshold, then the motion is classified as directed. (*D*) MSD versus time lag calculated for the portion of the trajectory from 1.5 to 3.75 s. The data were fit to a quadratic formula (see *SI Text*) yielding an estimated velocity of 768 nm/s.

as directed. This method enables us to extract the velocities and dwell times of specific portions of trajectories that satisfy explicit, objective criteria for directed motion, something that is not possible by more phenomenological approaches. The calculation of the SCI in three dimensions and the corresponding threshold selection procedure are described in detail in *SI Text*.

We calculated the SCI and identified periods of apparent directed motion for all observed trajectories with more than 200 time points. Fig. 4*A* shows the distribution of dwell times for untreated cells, latrunculin B-treated cells, and Brownian simulations using average diffusion coefficients and localization-precision parameters from the untreated cell experiments. Although the distributions of dwell times were similar for the three conditions, the distribution was shifted toward longer dwell times for the untreated *ARG3* cells. Dwell times were reduced, and the presence of apparent directed motion did not differ significantly from Brownian simulation by treatment with latrunculin B. The maximum dwell time for directed motion of *ARG3* mRNA was reduced from 2.2 s for untreated cells to 0.93 s for the latrunculin B-treated cells. The mean values of the dwell time for the untreated, latrunculin B-treated cells, and simulation data were 0.42 ± 0.49 s, 0.28 ± 0.24 s, and 0.35 ± 0.33 s, respectively. The rare long intervals of directed motion (>1 s) observed in the untreated cells are likely dependent on actin filaments because they do not appear in the corresponding latrunculin B-treated cells. The overall similarity of the dwell time distributions, however, suggests that the majority of the intervals of apparent directed motion are not due to transport along actin cables but rather are false positives that also occur in Brownian-motion.

Quantitative predictions from specific mechanistic models for directed transport can be tested by comparing such predictions to observed distributions of velocities and dwell times (24, 56). In previous studies of *ASH1* transport in yeast, mRNP particles exhibited directed motion with average velocities of 200–400 nm/s, which was interpreted as consistent with transport by Myo4 along actin cables (33). We estimated velocities during directed motion events from the second-order coefficient obtained from quadratic fits to the MSD curve (see Fig. 3*D* and *SI Text*) to yield the distribution shown in Fig. 4*B*. SCI analysis is not efficient at detecting directed portions with a length less than 10 exposure times (0.15 s) (24). To ensure statistically significant velocity measurements, we therefore analyzed only directed portions with lengths greater than 0.48 s (see *SI Text*) (9, 20, 24), which precluded a statistically significant distribution of velocities for the latrunculin B-treated cells. The mean velocity of directed trajectories observed in the untreated cells was 380 ± 210 nm/s ($n = 31$). Although this value is broadly consistent with actomyosin-based transport, further experiments will be needed to determine the actual mechanisms of these directed movements. Quantitative analyses such as SCI determinations will be a powerful tool for interpreting the effects of specific mutations or chemical inhibitors on studies of directed transport using high-resolution 3D imaging.

Confinement

In 1993, Saxton (21) proposed an algorithm to measure confinement in experimental trajectories that was later experimentally implemented by Simson, et al. (48). The test is based on the probability that a purely random diffuser would stay within a given two-dimensional radius given a diffusion coefficient and observation time window. To implement this test, one has to divide the complete trajectory into many subtrajectories of time, t_w, and then determine a maximum value of displacement, R, for each subtrajectory. This maximum value of R, the diffusion coefficient D, and the subtrajectory time window, t_w, are used to calculate the probability, Ψ, that a random walk would stay within a circle of that radius. A threshold probability is set by simulation and is typically chosen such that only 5% simulated random walks would be considered confined. The measured probability is then compared to the threshold, and the subtrajectory is considered confined for times where the calculated probability is less than the threshold. We developed a 3D version of this test (analytical expressions for Ψ as a function of D, R, and t_w can be found in *SI Text*). In order to visualize the changes in Ψ, it is best to plot $\log(\Psi)$. Numerically, $\log(\Psi)$ can be approximated as a linear function of Dt/R^2,

$$\log(\Psi) = 0.301 - 4.286(Dt_w/R^2). \quad [2]$$

Fig. 5 shows a representative example of an experimentally observed trajectory in which confinement was detected using Eq. **2**. The average D value for this trajectory was 0.0087 $\mu m^2/s$, and the mean localization precision was 12 nm. Although different values of the window time t_w can be chosen, here we choose 50 time steps (0.75 s) for simplicity; analysis with 40 or 60 time steps gave similar results. Five thousand simulations were run, each with 1,000 time steps, to obtain a threshold value for $\log(\Psi)$ of −1.64. The trajectory and the plot of $\log(\Psi)$ in Fig. 5 are both color-coded to represent time, and confinement was observed during time intervals 0.375 to 1.035 s, 2.475 to 3.840 s, and 6.855 to 7.050 s.

The distribution of confinement test radii R and corresponding dwell times in confining regions has the potential to provide information about the molecular interactions that occur between the mRNP and structures inside the cell. Fig. 6 shows the observed distribution of confinement sizes and dwell times for all analyzed trajectories along with Brownian simulations with the same distribution of diffusion coefficients and localization precisions observed in the data. Note that the precise values for these parameters, especially the confinement radii, depend upon the choice of threshold and window size (48) as well as other considerations (57, 58). Mean confinement test radii of 190 ± 94 nm and 244 ± 100 nm were obtained from experimen-

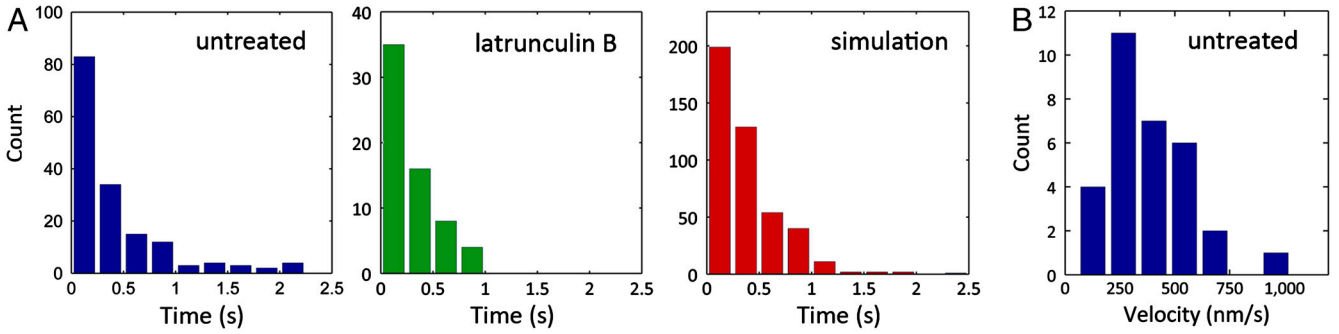

Fig. 4. Dwell times and velocities for directed subtrajectories can be extracted using an SCI analysis. (*A*) Distribution of directed dwell times for the untreated cells, latrunculin B-treated cells and Brownian simulations. (*B*) Velocities extracted from all directed portions of tracks longer than 0.48 s in the untreated case (see *SI Text*).

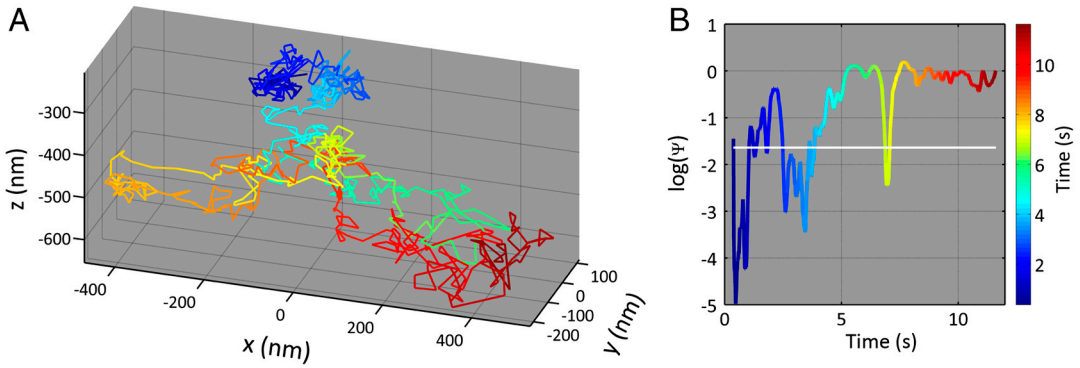

Fig. 5. Transient three-dimensional confinement in an experimental trajectory can be detected using Eq. **2**. (*A*) Representative trajectory displaying transient three-dimensional confinement. Time is encoded as color in the color bar in *B*. (*B*) The log of the probability that a unobstructed diffusive particle would stay within a given radius, $\log(\Psi)$, plotted as a function of time for the trajectory in *A*. Three separate transient confinement regions are detected. The white line is the threshold described in the text.

tal and simulated data, respectively. For a particle with a diffusion coefficient of 0.039 $\mu m^2/s$, the average root mean square displacement in a time window of 0.75 s (fifty 15-ms time steps) is 420 nm, but the simulated distribution shows how even the Brownian diffuser can linger in smaller regions from time to time. Because of the large widths of both distributions in Fig. 6*A*, it is not possible to declare a significant difference between them. However, the mean dwell time derived from the Brownian diffuser simulation, 0.15 ± 0.1 s, was significantly shorter than the mean dwell time derived from the experimental data, 0.28 ± 0.4 s. The excess of long confinement times observed in the experimental data compared to the random diffusion model suggests the possibility of interactions between the *ARG3* mRNP and a cellular structure, such as an organelle, cytoskeletal structure, or subcellular compartment. Using Eq. **2** to explicitly classify localized mRNPs and investigating the effects of perturbing hypothetical interacting structures or molecules on the frequency and duration of mRNP localization could be a powerful method for defining and testing quantitative models for the molecular nature and physical characteristics of the interactions.

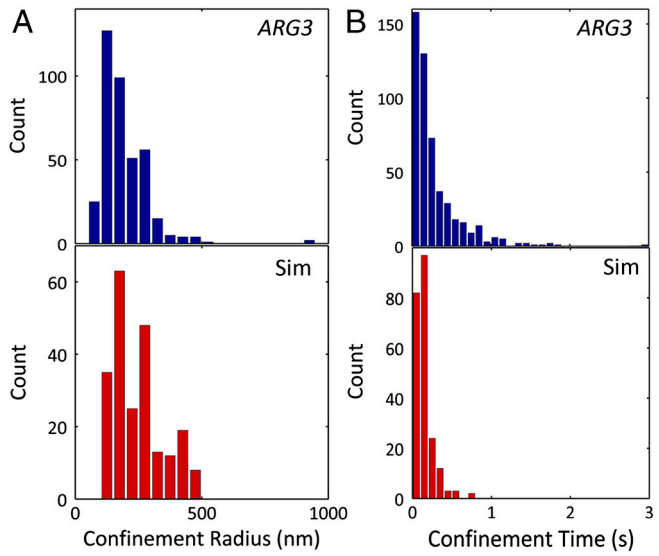

Fig. 6. The confinement radii *R* and confinement times can be measured from the confined subtrajectories identified using Eq. **2**. (*A*) Confinement radii measured from all trajectories with more than 200 time steps and the corresponding confinement radii which would occur from Brownian motion. (*B*) Dwell times of confined subtrajectories for experimental data and simulations. Note the higher density at larger values of confinement time in the experimental data.

Conclusion

Our investigation of the dynamics of a specific mRNA in living yeast cells provides an illustration of how much can be learned from an objective and quantitative analysis of data from 3D single-particle tracking with the DH-PSF microscope. We have described explicit, unbiased, statistical tests to distinguish between random, confined, and directed modes of motion and applied them to interpretation of experimental measurements of the motion of the *ARG3* mRNA in living yeast. The results show that for this mRNA, which is not known to be localized to a particular cellular compartment, most of the movements are consistent with random diffusion, but a small proportion of the trajectories appear to be nonrandom, including periods in which the mRNA appears stationary, confined, and consistent with directed transport. The techniques and results of this work can be used as a starting point for quantitative analysis of the dynamics and molecular mechanisms underlying the programmed localization of mRNA molecules in yeast and other organisms. We expect the methods described here to be of use not only in mRNA tracking experiments but also in quantitative 3D tracking of other fluorescently tagged structures in living cells, tissues, and ex vivo models.

Materials and Methods

Sample Preparation. JCY324 cells (see *SI Text* for strain construction and cell culture) were grown overnight in synthetic complete (SC) his– media supplemented with glucose (2% wt/vol final) and adenine hemisulfate (40 μg/mL final; SC his– glu+ ade+). Upon entry into early log phase, the cells were transferred into induction media lacking methionine (SC his– met– glu+ ade+) and allowed to grow at 30 °C for one to 3 h. Cells were then removed from the inducing media for 3 h before imaging to reduce the fluorescent MS2-EGFP background. Agarose pads composed of 1.5% wt/wt solid agarose [Sigma type 1-A, Low electroendosmosis (EEO)] dissolved in SC his– glu+ ade+ media were made by sandwiching between two plasma-etched 30 mm × 50 mm #1 glass coverslips (typically 175 μm thick) and then one coverslip was removed. The cells were then washed with fresh SC his– glu+ ade+ media three times and roughly 2 μL of 10× concentrated cells were deposited onto the pad. A plasma-etched 25 mm × 25 mm glass coverslip was placed on top of the cells to form the imaging interface. The sample was then sealed with paraffin wax. Because the stage drift in the microscope during the time scale of our experiments (5–10 s) is negligible compared to the motion of the mRNPs, fiduciary markers were not used. Immobilizing the cells on agarose was found to be far superior to polylysine-coated coverslips in preventing cell motion, although a higher background resulted from illumination through the gel.

Microscopy. The samples were mounted on an inverted Olympus IX71 fluorescence microscope. The microscope was fitted with a DH-PSF image processing section on the left output port. The DH-PSF imaging system has been described in detail previously (27, 59). The EGFP was excited with an Ar-ion laser emitting at 488 nm with an irradiance of 0.5 kW/cm^2. The laser was aligned at a high angle in a "quasi-total internal reflection fluor-

escence" geometry to reduce background but not restrict excitation to a region thinner than the yeast cells (60). The emission was filtered with a Chroma Z488RDC dichroic and a Chroma HQ525/50 band-pass filter with a transmission band from 500–550 nm. It was found that the 488-nm laser-excited yellow fluorescence in the yeast and the rejection of wavelengths longer than 550 nm greatly enhanced the signal-to-background ratio in the images. Images of 128×128 pixels were acquired on an Andor iXon^{+} electron multiplying CCD with a 15-ms exposure time. Although the camera can be run with a 7.5-ms exposure time with a 128×128 image size, we found that 15 ms is fast enough to define the dynamics while collecting enough light to obtain acceptable signal to noise in the images.

Image Analysis. In each image, a presumptive mRNP is identified by hand and localized using a least-squares fitting scheme to the sum of two Gaussian functions as described previously (27). The midpoint between the two lobes of the DH-PSF denotes the lateral position of the mRNP and the angle between the two lobes denotes the *z* position. Trajectories were all checked by eye to ensure that the fitting program was working properly and no egregious localizations remained in the trajectory. More details on the fitting algorithm can be found in *SI Text*. A calibration of angle versus *z* position was performed by moving 200-nm fluorescent beads (Invitrogen Fluospheres 505/515) immobilized in 1% poly(vinyl alcohol) on a glass coverslip using an objective *z* positioner (PIFOC *p*-721.CDQ stage with E625.CO analog controller, Physik Instrumente). More details on the calibration of the DH-PSF imaging system can be found in previous work (27, 59). Because of the index mismatch between the immersion oil of the objective ($n = 1.518$) and the yeast cytoplasm ($n\sim = 1.38$), the true *z* position differs from the measured *z* position of the mRNP (61, 62). Because it is not currently possible to precisely model the effects of index mismatch on the DH-PSF imaging system, a unique procedure for correcting the combined effects of focal shift and spherical aberration based on the measured short-time diffusion coefficients in all three dimensions has been developed and is described in *SI Text*. Details on the Brownian Monte Carlo simulations for the statistical tests are also provided in *SI Text*.

ACKNOWLEDGMENTS. We thank R. Piestun for providing the DH-PSF phase mask. The receipt of MATLAB code for the calculation of the two-dimensional speed correlation index from Dr. C. Bouzigues and Prof. M. Dahan is gratefully acknowledged, as is the receipt of the MS2-tagging plasmids from Dr. J. Gerst. We thank Matthew Lew for helpful discussions. This work was supported in part by Grant R01GM085437 from the National Institute of General Medical Sciences (to W.E.M) and grants R01CA77097 and R01CA111487 from the National Institutes of Health (to P.O.B.). M.A.T. acknowledges support from a National Science Foundation Graduate Research Fellowship and a Bert and DeeDee McMurtry Stanford Graduate Fellowship. J.M.C. acknowledges the Jane Coffin Childs Memorial Research Fund for a postdoctoral fellowship. P.O.B. is an investigator of the Howard Hughes Medical Institute.

1. Moerner WE, Kador L (1989) Optical detection and spectroscopy of single molecules in a solid. *Phys Rev Lett* 62:2535–2538.
2. Gräslund A, Rigler R, Widengren J, eds. (2010) *Single Molecule Spectroscopy in Chemistry, Physics, and Biology: Nobel Symposium*Springer Series in Chemical Physics (Springer, Berlin), Vol 96, pp 1–572.
3. Selvin PR, Ha T, eds. (2008) *Single-Molecule Techniques: A Laboratory Manual* (Cold Spring Harbor Lab Press, Cold Spring Harbor, NY), pp 1–507.
4. Xie XS, Choi PJ, Li GW, Lee NK, Lia G (2008) Single-molecule approach to molecular biology in living bacterial cells. *Annu Rev Biophys* 37:417–444.
5. Lord SJ, Moerner WE (2010) Single-molecule spectroscopy and imaging of biomolecules in living cells. *Anal Chem* 82:2192–2203.
6. Barak LS, Webb WW (1982) Diffusion of low density lipoprotein-receptor complex on human fibroblasts. *J Cell Biol* 95:846–852.
7. Gelles J, Schnapp BJ, Sheetz MP (1988) Tracking kinesin-driven movements with nanometre-scale precision. *Nature* 4:450–453.
8. Schmidt T, Schuetz GJ, Baumgartner W, Gruber HJ, Schindler H (1995) Characterization of photophysics and mobility of single molecules in a fluid lipid membrane. *J Phys Chem* 99:17662–17668.
9. Kusumi A, Sako Y, Yamamoto M (1993) Confined lateral diffusion of membrane receptors as studied by single particle tracking (nanovid microscopy). Effects of calcium-induced differentiation in cultured epithelial cells. *Biophys J* 65:2021–2040.
10. Goulian M, Simon SM (2000) Tracking single proteins within cells. *Biophys J* 79:2188–2198.
11. Harms GS, et al. (2001) Single-molecule imaging of L-type Ca^{2+} channels in live cells. *Biophys J* 81:2639–2646.
12. Dahan M, et al. (2003) Diffusion dynamics of glycine receptors revealed by single-quantum dot tracking. *Science* 302:442–445.
13. Douglass AD, Vale RD (2005) Single-molecule microscopy reveals plasma membrane microdomains created by protein-protein networks that exclude or trap signaling molecules in T cells. *Cell* 121:937–950.
14. Vrljic M, Nishimura SY, Brasselet S, Moerner WE, McConnell HM (2002) Translational diffusion of individual class II MHC membrane proteins in cells. *Biophys J* 83:2681–2692.
15. Nishimura SY, Vrljic M, Klein LO, McConnell HM, Moerner WE (2006) Cholesterol depletion induces solid-like regions in the plasma membrane. *Biophys J* 90:927–938.
16. Vrljic M, Nishimura SY, Moerner WE (2007) Single-molecule tracking. *Methods Mol Biol* 398:193–219.
17. Umemura YM, et al. (2008) Both MHC class II and its GPI-anchored form undergo hop diffusion as observed by single-molecule tracking. *Biophys J* 95:435–450.
18. Wieser S, Schütz GJ (2008) Tracking single molecules in the live cell plasma membrane —Do's and Don't's. *Methods* 46:131–140.
19. Braeuchle C, Lamb DC, Michaelis J, eds. (2010) *Single Particle Tracking and Single Molecule Energy Transfer* (Wiley-VCH, Weinheim, Germany), pp 1–343.
20. Qian H, Sheetz MP, Elson EL (1991) Single particle tracking. Analysis of diffusion and flow in two-dimensional systems. *Biophys J* 60:910–921.
21. Saxton MJ (1993) Lateral diffusion in an archipelago. *Biophys J* 64:1766–1780.
22. Saxton MJ, Jacobson K (1997) Single-particle tracking: Applications to membrane dynamics. *Annu Rev Biophys Biomol Struct* 26:373–399.
23. Savin T, Doyle PS (2005) Static and dynamic errors in particle tracking microrheology. *Biophys J* 88:623–638.
24. Bouzigues C, Dahan M (2007) Transient directed motions of GABAA receptors in growth cones detected by a speed correlation index. *Biophys J* 92:654–660.
25. Pavani SRP, Greengard A, Piestun R (2009) Three-dimensional localization with nanometer accuracy using a detector-limited double-helix point spread function system. *Appl Phys Lett* 95:021103.
26. Pavani SRP, Piestun R (2008) High-efficiency rotating point spread functions. *Opt Express* 16:3484–3489.
27. Thompson MA, Lew MD, Badieirostami M, Moerner WE (2010) Localizing and tracking single nanoscale emitters in three dimensions with high spatiotemporal resolution using a double-helix point spread function. *Nano Lett* 10:211–218.
28. Martin KC, Ephrussi A (2009) mRNA localization: Gene expression in the spatial dimension. *Cell* 136:719–730.
29. Gerber AP, Herschlag D, Brown PO (2004) Extensive association of functionally and cytotopically related mRNAs with puf family RNA-binding proteins in yeast. *PLoS Biol* 2:e79.
30. Lecuyer E, et al. (2007) Global analysis of mRNA localization reveals a prominent role in organizing cellular architecture and function. *Cell* 131:174–187.
31. Zimyanin VL, et al. (2008) In vivo imaging of oskar mRNA transport reveals the mechanism of posterior localization. *Cell* 134:843–853.
32. Vargas DY, Raj A, Marras SAE, Kramer FR, Tyagi S (2005) Mechanism of mRNA transport in the nucleus. *Proc Natl Acad Sci USA* 102:17008–17013.
33. Bertrand E, et al. (1998) Localization of ASH1 mRNA particles in living yeast. *Mol Cell* 2:437–445.
34. Takizawa PA, Vale RD (2000) The myosin motor, Myo4p, binds Ash1 mRNA via the adapter protein, She3p. *Proc Nat Acad Sci USA* 97:5273–5278.
35. Chartrand P, Meng XH, Huttelmaier S, Donato D, Singer RH (2002) Asymmetric sorting of Ash1p in yeast results from inhibition of translation by localization elements in the mRNA. *Mol Cell* 10:1319–1330.
36. Holstege FCP, et al. (1998) Dissecting the regulatory circuitry of a eukaryotic genome. *Cell* 95:717–728.
37. Zenklusen D, Larson DR, Singer RH (2008) Single-RNA counting reveals alternative modes of gene expression in yeast. *Nat Struct Mol Biol* 15:1263–1271.
38. Haim L, Zipor G, Aronov S, Gerst JE (2007) A genomic integration method to visualize localization of endogenous mRNAs in living yeast. *Nat Methods* 4:409–412.
39. Lange S, et al. (2008) Simultaneous transport of different localized mRNA species revealed by live-cell imaging. *Traffic* 9:1256–1267.
40. Cang H, Wong CM, Xu CS, Rizvi AH, Yang H (2006) Confocal three dimensional tracking of a single nanoparticle with concurrent spectroscopic readouts. *Appl Phys Lett* 88:223901.
41. McHale K, Berglund AJ, Mabuchi H (2007) Quantum dot photon statistics measured by three-dimensional particle tracking. *Nano Lett* 7:3535–3539.
42. Levi V, Ruan QQ, Gratton E (2005) 3-D particle tracking in a two-photon microscope: Application to the study of molecular dynamics in cells. *Biophys J* 88:2919–2928.
43. Ram S, Prabhat P, Chao J, Ward ES, Ober RJ (2008) High accuracy 3D quantum dot tracking with multifocal plane microscopy for the study of fast intracellular dynamics in live cells. *Biophys J* 95:6025–6043.
44. Kao HP, Verkman AS (1994) Tracking of single fluorescent particles in three dimensions: Use of cylindrical optics to encode particle position. *Biophys J* 67:1291–1300.
45. Sun Y, McKenna JD, Murray JM, Ostap EM, Goldman YE (2009) Parallax: High accuracy three-dimensional single molecule tracking using split images. *Nano Lett* 9:2676–2682.
46. Spector I, Shochet NR, Blasberger D, Kashman Y (1989) Latrunculins—novel marine macrolides that disrupt microfilament organization and affect cell growth: I. comparison with cytochalasin D. *Cell Motil Cytoskeleton* 13:127–144.
47. Spector I, Shochet NR, Kashman Y, Groweiss A (1983) Latrunculins: Novel marine toxins that disrupt microfilament organization in cultured cells. *Science* 219:493–495.
48. Simson R, Sheets ED, Jacobson K (1995) Detection of temporary lateral confinement of membrane proteins using single-particle tracking analysis. *Biophys J* 69:989–993.
49. Saxton MJ (1997) Single-particle tracking: The distribution of diffusion coefficients. *Biophys J* 72:1744–1753.
50. Montiel D, Cang H, Yang H (2006) Quantitative characterization of changes in dynamical behavior for single-particle tracking studies. *J Phys Chem B* 110:19763–19770.
51. Shav-Tal Y, et al. (2004) Dynamics of single mRNPs in nuclei of living cells. *Science* 304:1797–1800.

52. Moore MJ (2005) From birth to death: The complex lives of eukaryotic mRNAs. *Science* 309:1514–1518.
53. Fusco D, et al. (2003) Single mRNA molecules demonstrate probabilistic movement in living mammalian cells. *Curr Biol* 13:161–167.
54. Weiss M, Elsner M, Kartberg F, Nilsson T (2004) Anomalous subdiffusion is a measure for cytoplasmic crowding in living cells. *Biophys J* 87:3518–3524.
55. Golding I, Cox EC (2006) Physical nature of bacterial cytoplasm. *Phys Rev Lett* 96:098102.
56. Saxton MJ (1994) Single-particle tracking: Models of directed transport. *Biophys J* 67:2110–2119.
57. Destainville N, Salome L (2006) Quantification and correction of systematic errors due to detector time-averaging in single-molecule tracking experiments. *Biophys J* 90:L17–L19.
58. Wieser S, Moertelmaier M, Fuertbauer E, Stockinger H, Schütz GJ (2007) (Un)confined diffusion of CD59 in the plasma membrane determined by high-resolution single molecule microscopy. *Biophys J* 92:3719–3728.
59. Pavani SRP, et al. (2009) Three-dimensional, single-molecule fluorescence imaging beyond the diffraction limit by using a double-helix point spread function. *Proc Nat Acad Sci USA* 106:2995–2999.
60. Cui B, et al. (2007) One at a time, live tracking of NGF axonal transport using quantum dots. *Proc Nat Acad Sci USA* 104:13666–13671.
61. Deng Y, Shaevitz JW (2009) Effect of aberration on height calibration in three-dimensional localization-based microscopy and particle tracking. *Appl Opt* 48:1886–1890.
62. Huang B, Jones SA, Brandenburg B, Zhuang X (2008) Whole-cell 3D STORM reveals interactions between cellular structures with nanometer-scale resolution. *Nat Methods* 5:1047–1052.